


# Stimulus Responsive Nanocarrier for Enhanced Antitumor Responses Against Hepatocellular Carcinoma

Deteng Zhang<sup>1-4</sup>, Jinxiao Song<sup>4</sup>, Zhenghui Jing<sup>4</sup>, Huan Qin<sup>4</sup>, You Wu<sup>3</sup>, Jingyi Zhou<sup>4</sup>, Xinlong Zang<sup>1-4</sup> 

<sup>1</sup>The Affiliated Hospital of Qingdao University, Qingdao University, Qingdao, Shandong, People's Republic of China; <sup>2</sup>Qingdao Cancer Institute, Qingdao University, Qingdao, People's Republic of China; <sup>3</sup>Institute of Neuroregeneration and Neurorehabilitation, Qingdao University, Qingdao, People's Republic of China; <sup>4</sup>School of Basic Medicine, Qingdao Medical College, Qingdao University, Qingdao, People's Republic of China

Correspondence: Xinlong Zang, Email zangxinlong@126.com

**Background:** Hepatocellular carcinoma (HCC) is a serious global health concern, accounting for about 90% of all liver cancer instances. Surgical treatment is a fundamental aspect of HCC management; however, the challenge of postoperative recurrence significantly impacts mortality rates.

**Methods:** We have developed a pH and reactive oxygen species (ROS) dual stimulus-responsive drug delivery system (PN@GPB-PEG NPs) loaded with chemotherapeutic paclitaxel (PTX) and indoleamine 2,3-dioxygenase (IDO) inhibitor NLG919, for HCC chemoimmunotherapy. The physiochemical properties, such as particle size, zeta potential, morphology, and encapsulation efficiency, were characterized. Furthermore, we investigated in vitro cytotoxicity, cellular uptake and immunogenic cell death in tumor cells treated with our nanoparticles. In vivo biodistribution, antitumor effects and immune responses were assessed in an HCC mice model.

**Results:** PN@GPB-PEG NPs display pH-responsive properties with improved targeting abilities toward tumors and improved uptake by HCC cells. Upon exposure to oxygen peroxide (H<sub>2</sub>O<sub>2</sub>), the sophisticated design allows for rapid release of therapeutic agents. In this process, PTX induces immunogenic cell death (ICD), which activates the immune system to generate an antitumor response. Simultaneously, NLG919 works to inhibit IDO, mitigating the immunosuppressive environment. This combination strategy leverages the advantages of both chemotherapy and immunotherapy, resulting in a powerful synergistic antitumor effect. In a mouse model of HCC, our nanoparticles effectively inhibited the growth of primary and recurrent tumors.

**Conclusion:** These encouraging results highlight the potential of our nanocarrier system as an innovative therapeutic approach to address HCC primary tumor and postsurgical recurrence, providing hope for enhanced patient outcomes.

**Keywords:** hepatocellular carcinoma (HCC), nanoparticles, stimuli responsiveness, chemoimmunotherapy, paclitaxel (PTX), NLG919

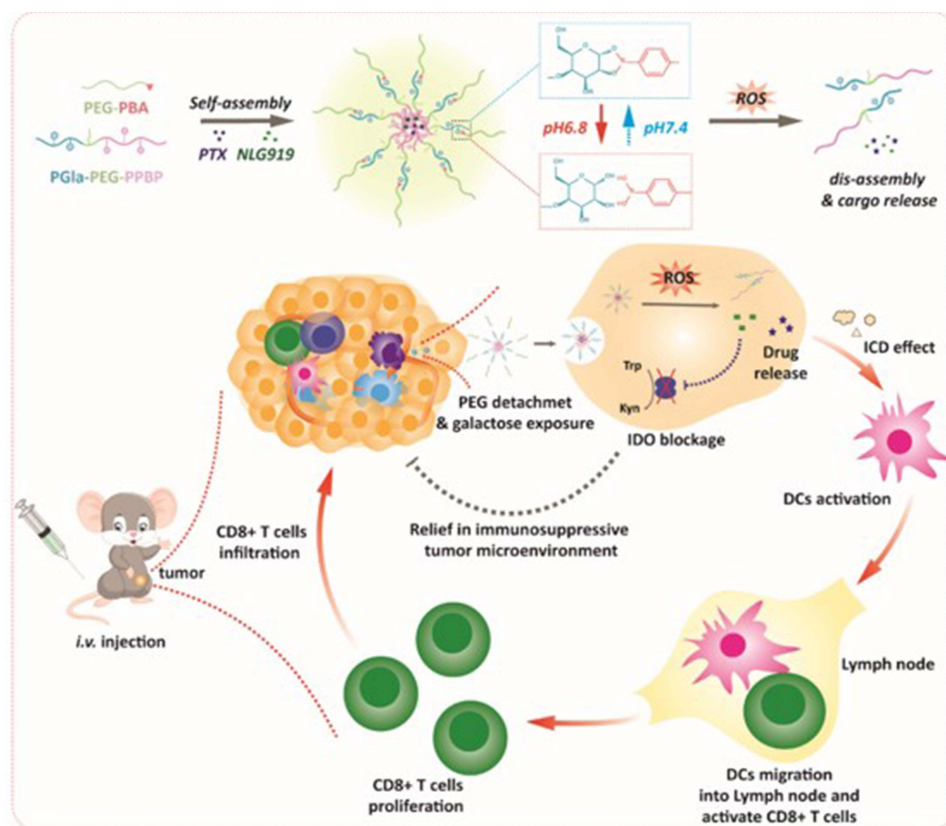
## Introduction

Hepatocellular carcinoma (HCC) remains a predominant form of liver cancer with relative 18% five-year survival rate.<sup>1,2</sup> The insidious HCC often results in patients being diagnosed at intermediate or advanced stages.<sup>3</sup> Despite notable progress in surgical resection techniques, approximately 70% of patients experience HCC recurrence within 5 years.<sup>4</sup> While other treatment modalities, including embolization and radiotherapy, are available, around half of HCC patients undergo chemotherapy at some point during their treatment.<sup>5</sup> Recently anti-PD-1/PD-L1, anti-CTLA-4 and anti-LAG-3 antibodies have demonstrated significant potential for tumor treatment; nevertheless, only a small subset of patients with HCC benefit from these immune checkpoint inhibitors.<sup>6</sup>

Importantly, some chemotherapeutic agents, such as mitoxantrone, doxorubicin, and paclitaxel (PTX), can eradicate tumor cells with improved immunogenicity, termed as immunogenic cell death (ICD).<sup>7</sup> In the process, tumor cells can upregulate calreticulin (CRT), high mobility group protein 1 (HMGB1) and adenosine triphosphate (ATP), etc., which can activate dendritic cells (DCs) and following effector T cells. These activated T cells subsequently infiltrate tumor tissues to eliminate cancer cells. However, these therapeutic agents potentially induce harmful immunosuppression and diminish CD8<sup>+</sup> T cells- and natural killer

cells (NKs)-mediated antitumor responses.<sup>8,9</sup> Notably, the interferon gamma (IFN- $\gamma$ ) mediated IDO overexpression plays a crucial role in the immunosuppressive tumor microenvironment (ITME).<sup>10</sup> For instance, IDO-mediated kynurenine (Kyn) accumulation led to immunosuppressive DCs differentiation and regulatory T cells (Tregs) recruitment and expansion.<sup>11</sup> Moreover, IDO upregulation can increase intratumoral tumor-associated macrophages (TAMs) and myeloid-derived suppressor cells (MDSCs).<sup>12</sup> These immunosuppressive cells, accompanied with anti-inflammatory cytokines and others, further weaken local immune responses. Although IDO inhibition alone may not yield effective antitumor effectiveness, IDO inhibitors like NLG919 significantly alleviate local immune suppression and restore antitumor immunity.<sup>11,13,14</sup> Therefore, it is crucial to synergistically induce ICD while modulating the ITME, which may tackle the shortcomings of single-agent therapy, ultimately achieving more efficient and favorable therapeutic outcomes.

It is challengeable to combine chemotherapeutic agents with immunomodulators with various pharmacokinetics, suboptimal tumor-targeting, and significant side adverse effects.<sup>15</sup> Nanotechnology offers promising avenues for the simultaneous delivery of various therapeutic agents.<sup>16–20</sup> In this study, we introduced a stimulus-responsive nanocarrier (PN@GPB-PEG NPs) loaded with chemotherapeutic paclitaxel (PTX) and indoleamine 2,3-dioxygenase (IDO) inhibitor NLG919 for HCC chemoimmunotherapy (Scheme 1). PN@GPB-PEG NPs were designed with significant responsiveness to changes in tumor microenvironmental pH and intracellular redox stimulus, thereby facilitating cellular uptake in tumor cells and intracellular cargo release. To realize these properties, PN@GPB-PEG NPs were developed with a “core-shell” structure. The “inner core” was polyacrylate derivatives composed of galactose, polyethylene glycol and phenyl boronate (PGal-PEG-PPBP) that can co-encapsulate PTX and NLG919 (termed PN@GPB NPs). Galactose of PGal acts as an effective ligand by binding to the asialoglycoprotein receptor (ASGP-R) present on HCC cells, facilitating targeted delivery.<sup>21</sup> The hydrophobic segments PPBP are designed to be cleaved in response to elevated levels of reactive oxygen



**Scheme 1** Schematic illustration of dual-stimulus responsive drug delivery system (PN@GPB-PEG NPs) for HCC chemoimmunotherapy. The nanocarrier can accumulate into tumor, where PEG-shielding and galactose exposure promote cellular uptake in HCC cells in response to weak acidic environment. Subsequently, intracellular reactive oxygen species (ROS) triggered cargo release, which evoked a good synergistic antitumor effect of the immunogenic cell death through paclitaxel (PTX) and inhibition of IDO activity by NLG919. Therefore, PN@GPB-PEG NPs boosted efficient antitumor immune responses meanwhile relieved immunosuppressive tumor microenvironment, reducing primary tumor burden and postoperative recurrence.

species (ROS) within tumor cells,<sup>22</sup> while PEG enhances the colloidal stability. The “outer shell” composed of phenyl boronic acid-PEG (PBA-PEG) was conjugated to the “inner core” through the formation of boronate ester bound that is cleavable in acidic conditions, which is common in many tumors, allowing the “inner core” to be released specifically. Our results demonstrated that PN@GPB-PEG NPs demonstrated high distribution in tumor tissues, effective cell uptake, and the release of PTX and NLG919 within HCC cells. Consequently, the combination of PTX-triggered immunogenic cell death (ICD) and NLG919-mediated IDO inhibition facilitated synergistic chemoimmunotherapy, significantly suppressing primary tumor and reducing postoperative tumor recurrence. These data suggest that this nanopatform serves as a proof-of-concept for the application of chemoimmunotherapy aimed at inhibiting primary tumor and preventing HCC recurrence.

## Materials and Methods

### Materials, Cells and Animals

PTX, NLG919, Nile red (NR), methacryloyl chloride, 2,2'-azobis(2-methylpropionitrile), and  $\beta$ -D-galactose pentaacetate were acquired from Shanghai Energy Chemical Co., Ltd. 4-carboxybenzeneboronic pinacol ester, TEA, CH<sub>3</sub>ONa, PEG (~2KDa), Poly(ethylene glycol) methacrylate (PEGMA), hydroxyethyl methacrylate, boron trifluoride diethyl etherate were sourced from Shanghai Macklin Biochemical Technology Co., Ltd (China). DMAP and DCC were obtained from Shanghai Aladdin Co., Ltd. Bide Pharmatech Co., Ltd. provided 2-(dodecylthiocarbonothioylthio)-2-methylpropionic acid (Shanghai, China). Red blood cell lysis buffer, dialysis bag (MW, 3.5KDa), DNase I and cell counting kit-8 (CCK-8) were acquired from the Beijing Solarbio Science & Technology Co., Ltd. (China). Collagenase IV was sourced from Beijing Psaitong Biotechnology Co., Ltd (China). Unless mentioned otherwise, other chemical reagents were from Sinopharm Chemical Reagent Co., Ltd.

Mouse Hepa 1–6 cells were sourced from ATCC (US) and cultured in DMEM supplemented with 10% FBS in a humidified incubator with an atmosphere of 5% CO<sub>2</sub>.

Female C57BL/6 and Balb/c mice were obtained from Pengyue (Jinan, China). All experimental protocols were conducted in line with guideline built by the Qingdao University Institutional Animal Care and Use Committee, which has sanctioned all animal experiments in this study. Hepa 1–6 cells were injected subcutaneously into the left flank to establish a hepatocellular carcinoma allograft mouse model.

### Preparation of Nanoparticles

Polymer PGal-PEG-PPBP and PBA-PEG were synthesized and characterized as described in supporting information. Next, PN@GPB-PEG nanoparticles were formulated through a straightforward dialysis technique. Specifically, 10mg PGal-PEG-PPBP, 3mg PBA-PEG, 0.8mg PTX, and 0.4mg NLG919 were mixed in 1mL DMSO, which was dialyzed against 10mM PBS for 24h to obtain PN@GPB-PEG NPs. Using the same method, PN@GPB NPs were formulated without PBA-PEG presence. Likewise, Nile red (NR) or 1.1-dioctadecyl-3,3,3,3-tetramethylindotricarbocyanine iodide (DiR) labelled nanoparticles were formulation using the same method.

### Characterization of Nanoparticles

The sizes and surface charge were evaluated using the dynamic light scattering (DLS) technique (Nano ZS90 device, Malvern Instruments, UK). The morphology was observed by transmission electronic microscope (TEM). Briefly, nanoparticles were added onto a copper mesh, treated with 2% PTA, and observed by TEM (JEM-2100, JEOL, JP).

For stimuli-responsiveness investigation, the resultant nanoparticles were incubated with different pH buffers in the presence or absence of 1mM H<sub>2</sub>O<sub>2</sub>, for a duration of 2 hours. Size variations were analyzed using TEM and DLS methods. For the determination of encapsulation efficiency (EE) and drug loading efficiency (DLE), the high performance liquid chromatography (HPLC) technique was adopted as described in earlier studies.<sup>23,24</sup> In brief, PN@GPB-PEG NPs (0.2 mL) and methanol (0.8 mL) were mixed, the concentrations of PTX and NLG919 were quantified at  $\lambda=227\text{nm}$  and  $\lambda=274\text{nm}$ . The encapsulation (EE) and drug loading efficiency (DLE) were computed using the appropriate formulas.

$$EE (\%) = \frac{w_1}{w_2} \times 100\%$$

$$DLE (\%) = \frac{w_1}{w_1 + w_3} \times 100\%$$

Where  $w_1$ ,  $w_2$  and  $w_3$  were the weight of loaded and feeded drugs, and nanocarriers.

In vitro release behavior was assessed by dialysis technique. Two-milliliter formulations were placed in a dialysis bag (MWCO, 3500Da) and submerged in 50mL PBS (pH 7.4 or pH 6.5), with or without the presence of 1mM H<sub>2</sub>O<sub>2</sub>. At predetermined time points, samples (2mL) were taken from an external PBS and replaced with a fresh medium and analyzed using the HPLC method as previously detailed.

## In vitro Cellular Uptake Assay

To assess the cellular uptake, we conducted flow cytometry and confocal laser scanning microscopy (CLSM) analyses. Tumor cells were plated in 6-well dishes and incubated with NR-labelled nanoformulations. After harvesting, tumor cells were test by flow cytometry using PE channel. To optical observe cellular uptake, Hepa 1–6 cells were placed on a confocal dish and NR labeled nanoparticles were introduced. After 4h incubation, these cells were stained with 4',6-diamidino-2-phenylindole (DAPI) and visualized using TCS SP8 CLSM (Leica, Germany).

## Cytotoxicity Assay

The cytotoxic effects of these formulations on tumor cells were assessed using the standard CCK-8 assay.  $1 \times 10^4$  tumor cells were plated in a 96-well format and cultured overnight. Various nanomedicines were then introduced and incubated for 24 and 48 hours. After CCK-8 solution addition, and the absorbance was measured using PerkinElmer multi-plate reader. The cell viability was determined using the equation.

$$Cell\ viability (\%) = \frac{A_2 - A_0}{A_1 - A_0} \times 100\%$$

Where  $A_2$ ,  $A_1$  and  $A_0$  were the absorbance of treated, control and blank wells, respectively.

For further cytotoxicity evaluation, live/dead staining was performed as described previously.<sup>25</sup> Tumor cells were treated with various nanomedicines, incubated with Calcein AM/PI solution (Beyotime, China), and observed using a Ti2-U fluorescence microscopy (Nikon, Japan).

To evaluate proapoptotic effect of different formulations, Annexin V-FITC-PI staining was performed.  $5 \times 10^6$  tumor cells were plated in a six-well dish and incubated with various formulations for additional 12 hours. Tumor cells were then collected, stained with Annexin-FITC-PI, and analyzed using flow cytometry.

## Immunogenicity Assay

To explore immunogenic cell death, the levels of CRT, HMGB1 and ATP were assessed. Tumor cells were plated in a 6-well dish and incubated for 24 hours. Various formulations (pH 7.4 or pH 6.5) were then introduced for 24 hours. These cells were collected for CRT analysis meanwhile, the supernatants were reserved for HMGB1 and ATP detection.

Bone marrow-derived dendritic cells (BMDCs) from C57BL/6 mice were harvested from the femurs and tibias. BMDCs were cultured in RPMI1640 medium supplemented with granulocyte-macrophage colony stimulating factor (GM-CSF, 10 ng/mL) and then co-incubated with Hepa 1–6 cells pre-subjected to various treatments for 24 hours. After anti-CD80, CD86, and MHC II antibody staining, these BMDCs were analyzed using flow cytometry.

Splenocytes were obtained from female C57BL/6 mouse and labeled with CFSE according to the manufacturer's instructions. The splenic cells were then incubated with the above BMDCs for additional 24 hours and analyzed by flow cytometry.

## IDO Activity Assay

To assess the inhibition of IDO, Hepa 1–6 cells were initially treated with 10 ng/mL IFN- $\gamma$  for 24 hours to promote the upregulation of IDO. Following incubation with various formulations, tumor cells were collected for an immunoblot assay, while the supernatants were gathered for Kyn concentration analysis via HPLC, as outlined in our previous study.<sup>11</sup>

## In vivo Imaging Assay

To assess in vivo biodistribution, 200  $\mu$ L DiR-labeled nanoformulations were administered to mice bearing Hepa 1–6 tumors via tail vein. The mouse was monitored on a PerkinElmer in vivo imaging system (IVIS, US). After mice sacrifice, the major organs (heart, liver, spleen, lung and kidney) and tumors were harvested and analyzed with IVIS at 48h.

## In vivo Antitumor Effects

To assess in vivo antitumor effect, a Hepa 1–6 tumor bearing mouse model was developed. After inoculating the tumors for 7 days, the mice were intravenously injected with different formulations at a dose of 2mg/Kg. Tumor dimensions and body weight were recorded every 3 days. The tumor volume was determined using the following equation: Tumor volume ( $\text{mm}^3$ ) = longer diameter (L)  $\times$  shorter diameter (W)<sup>2</sup>/2. On the 15th day, tumor tissues were excised, weighed, and fixed in 4% paraformaldehyde for further pathohistological evaluation. Furthermore, survival rates were calculated based on the number of mice that survived following the cessation of treatment.

## Hematoxylin-Eosin (HE) and Immunohistochemistry (IHC) Staining

To examine the histopathological alterations, tumors from various treatment groups underwent HE and IHC staining. Tumor samples were sectioned and incubated with CRT, terminal-deoxynucleotidyl transferase mediated nick end labeling (TUNEL), and Ki67 antibodies, followed by secondary antibody treatment and DAPI staining. Moreover, tumor sections were processed for HE staining following standard protocols.

## In vivo Immune Responses

To explore the immune responses, we processed tumor tissues and tumor draining lymph nodes (TDLN) into single-cell suspensions. These cells were subsequently labeled with antibody combinations: DCs (CD11c-APC, CD80-FITC and CD86-PE), MDSCs (CD11b-PE and Gr-1-APC), TAMs (F4/80-APC and CD206-PE), Tregs (CD4-FITC, CD25-APC, and FoxP3-PE), activated T cells (CD8-APC and IFN- $\gamma$ -PE) and CD8+ T cells (CD3+CD8-APC).

## Anti-Postoperative Recurrence

To evaluate the effectiveness of PN@GPB-PEG NPs in preventing tumor recurrence, we established an incomplete tumor resection model.<sup>26</sup> Hepa 1–6 cells were inoculated into the axilla of C57BL/c mice and once the tumor volume was above 100 $\text{mm}^3$ , the tumor tissues were removed by surgery and subjected to different interventions. Tumor volume were monitored every 3 days. Splenocytes were harvested and labelled for flow cytometry analysis.

## Biosafety Evaluation

Healthy mice were randomly assigned to four groups and received different injections every 3 days for a total of five administrations. Meanwhile, bodyweight was recorded. Finally, major organs were harvested for HE staining.

## Statistical Analysis

All experiments were conducted at least three times, with results presented as mean  $\pm$  standard deviation (SD). Statistical comparisons were carried out using one-way and two-way ANOVA tests. Kaplan–Meier curves were utilized to assess overall survival across different groups. Statistical significance was defined as \*P < 0.05, \*\*P < 0.01, \*\*\*P < 0.001, \*\*\*\*P < 0.0001. Each experiment was repeated in triplicate.

## Results and Discussion

### Synthesis and Characterization of Copolymers

The synthesis of PGal-PEG-PPBP was carried out using reversible addition-fragmentation chain transfer (RAFT) polymerization (Figure S1A).  $^1\text{H}$  NMR spectrum of the copolymer and immediate products were shown in Figure 1 and Figure S2–S6. The key peaks for PGal-PEG-PPBP were observed at  $\delta_{\text{r-s}}=7.6\text{--}7.3$  (phenyl),  $\delta_{\text{a-h}}=3.5\text{--}5.2$  (galactose),  $\delta_{\text{t}}=1.28$  ( $-\text{CH}_3$ ), and  $\delta_{\text{k}}=0.78\text{--}1.1$  ppm ( $-(\text{CH}_2)_{10}\text{CH}_3$ ). In contrast, the disappearance of the peak at  $\delta=2.04$  signified the removal of the acetate protecting group. The synthesis of the coating material, PBA-PEG, was carried out via an ester formation reaction (Figure S1B). The typical peaks of  $\delta_{\text{y}}=3.6$  ppm (PEG),  $\delta_{\text{w}}=6.55$  and  $\delta_{\text{x}}=8.37$  ppm (PBA) confirmed the successful synthesis PBA-PEG (Figure 1B).

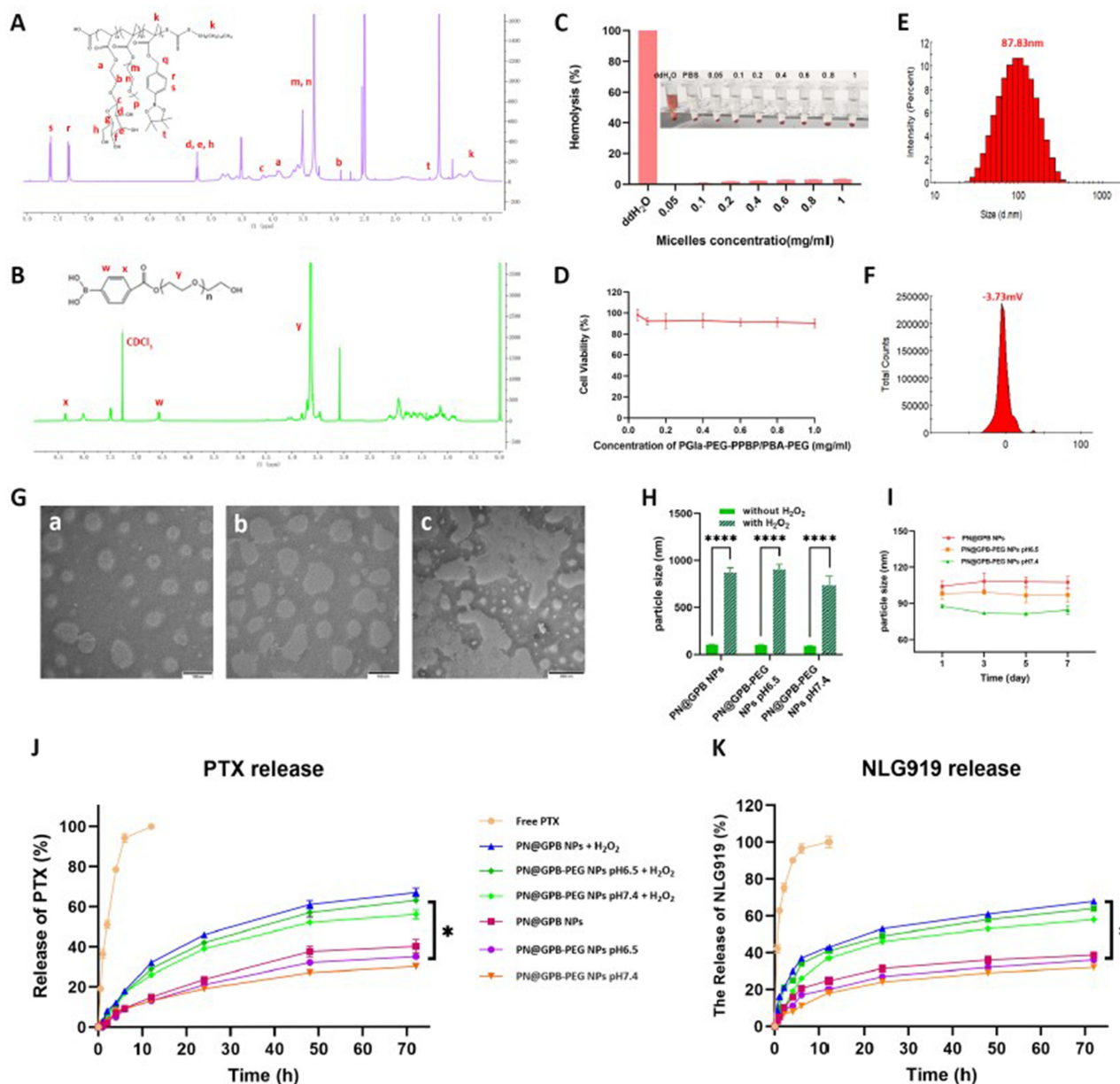


**Figure 1** Characterization of copolymers and nanoparticles. (A and B)  $^1\text{H}$  NMR of PGal-PEG-PPBP and PEG-PBA. (C) Hemolytic assay and representative image of erythrocytes cultured with blank nanoparticles composed of PGal-PEG-PPBP and PEG-PBA. (D) In vitro cytotoxicity of blank nanoparticles composed of PGal-PEG-PPBP and PEG-PBA against Hepa1-6 cells. (E and F) Diameter and zeta potential of PN@GPB-PEG NPs at pH7.4. (G) TEM images of PN@GPB-PEG NPs at pH7.4 (a) and pH6.5 (b), and 1mM  $\text{H}_2\text{O}_2$  (c). Scale bar=100 nm (a and b) or 200 nm (c). (H) Average particle sizes of PN@GPB-PEG NPs at different pH and redox conditions. (I) Stability of different nanoformulations at storage. (J and K) PTX and NLG919 release from PN@GPB-PEG NPs in different medium for 72h. \* $P<0.05$ .

The biocompatibility of these copolymers was assessed by hemocompatibility tests. As shown in [Figure 1C](#), the nanomaterials with concentration ranging from 0.05 to 1mg/mL exhibited only slight hemolysis ratios. Additionally, blank nanocarriers composed of PGal-PEG-PPBP and PEG-PBA displayed no significant inhibitory effects on Hepa 1–6 cells ([Figure 1D](#)). The results point to low inhibitory effects and good biocompatibility of the copolymers.

## Characterization of Nanoparticles

The resultant nanoparticles were synthesized through a straightforward dialysis technique, as previously outlined.<sup>27</sup> In an aqueous environment, PGal-PEG-PPBP and PBA-PEG were able to create nanoassemblies (PN@GPB-PEG NPs) that facilitated the inclusion of PTX and NLG919 into their hydrophobic cores. The particle size, zeta potential, and morphology were initially assessed and the results were shown in [Figure 1](#) and [Table S1](#). PN@GPB-PEG NPs exhibited an average diameter of 87.83 nm with PDI of 0.193. Transmission electron microscopy (TEM) images revealed PN@GPB-PEG NPs with a spherical shape. PN@GPB NPs had a diameter of ~104 nm by DLS results. The observed reduction in diameter by 18 nm could be attributed to the enhanced hydrophilicity of the PEG-PBA “outer shell”. PN@GPB-PEG NPs displayed a surface charge of  $-3.73$  mV, more positive than the  $-14.7$  mV of PN@GPB NPs, indicating the influence of PBA binding with galactose.<sup>28</sup>

Subsequently, the EE and DLE were assessed by HPLC method. [Table S2](#) showed that PN@GPB-PEG NPs achieved EE of 69.5% and 55.6% for PTX and NLG919, comparable to that of PN@GPB NPs. Furthermore, both nanoparticle formulations exhibited similar DLE values, approximately 4% for PTX and 1% for NLG919.

PN@GPB-PEG NPs were engineered to disassemble and facilitate cargo release respond to internal stimulus. We first tracked diameter and appearance changes at various pH levels, with or without H<sub>2</sub>O<sub>2</sub> incubation. Over a period of 7 days, the average diameter of PN@GPB-PEG NPs remained largely unchanged during storage ([Figure 1I](#)). In contrast, we noted an approximately 11 nm increase in particle size in a mildly acidic environment ([Figure 1H](#)). Nonetheless, these nanoparticles appeared to be relatively stable, as indicated by TEM images ([Figure 1G](#)) and their loading capacity ([Table S2](#)). Noticeably, at pH 6.5, PN@GPB-PEG exhibited a diameter and zeta potential closely resembling those of PN@GPB nanoparticles, implying the de-shielding of PEG under the weakly acidic conditions ([Table S1](#)). However, the PN@GPB-PEG NPs displayed an irregular and swollen morphology under H<sub>2</sub>O<sub>2</sub> conditions, reaching a particle size of approximately 700 nm, indicating their disassembly under ROS conditions ([Figure 1G](#) and [H](#)).

We further explore cargo release at different pHs with or without H<sub>2</sub>O<sub>2</sub>, and the results were shown in [Figure 1J](#). At a neutral pH, a release rate of 30.1% for PTX was recorded over 72 hours, indicating that PN@GPB-PEG NPs maintain satisfactory stability in circulation. In acidic conditions, a marginally higher PTX release was observed, likely due to PEG detachment facilitating drug diffusion from the core. Conversely, H<sub>2</sub>O<sub>2</sub> treatment significantly enhanced PTX release, showing a 1.675-fold increase compared to neutral conditions over the same period. This enhancement is attributed to boronic esters cleavage in response to an oxidative stimuli, leading to the structural collapse, in line with observed changes in size and morphology.<sup>22</sup> [Figure 1K](#) exhibited that NLG919 release was improved upon H<sub>2</sub>O<sub>2</sub> incubation. These findings indicate that ROS facilitates PTX and NLG919 release, whereas a low pH does not.

## In vitro Cellular Uptake

To assess cellular uptake, PN@GPB-PEG NPs were labelled with Nile red (NR) and co-incubated with Hepa 1–6 cells. The results are illustrated in [Figure 2A](#) and [B](#). A comparison between NR@GPB-PEG NPs and NR@GPB NPs at pH 7.4 revealed that PEG shielding led to ~42% decrease in uptake by Hepa 1–6 cells, indicating that PEG coating hindered the interaction between galactose and ASGP-R. As anticipated, incubation at pH 6.5 significantly enhanced NR@GPB-PEG NPs uptake in Hepa 1–6 cells, suggesting that the acidic tumor microenvironment facilitated PEG detachment and exposure of galactose. Moreover, the fluorescence intensity increased in a time-dependent manner. To evaluate ASGR-dependent uptake in Hepa 1–6 cells, free galactose was added to blocking the receptor. As depicted in [Figure 2C](#), galactose pre-treatment markedly diminished the fluorescent intensity of NR@GPB-PEG NPs at pH 6.5. These findings indicate that the increased cellular uptake is driven by interactions between galactose and ASGR. CLSM observations shown in [Figure 2D](#) illustrated that a mildly acidic environment significantly promoted NR@GPB-PEG NPs

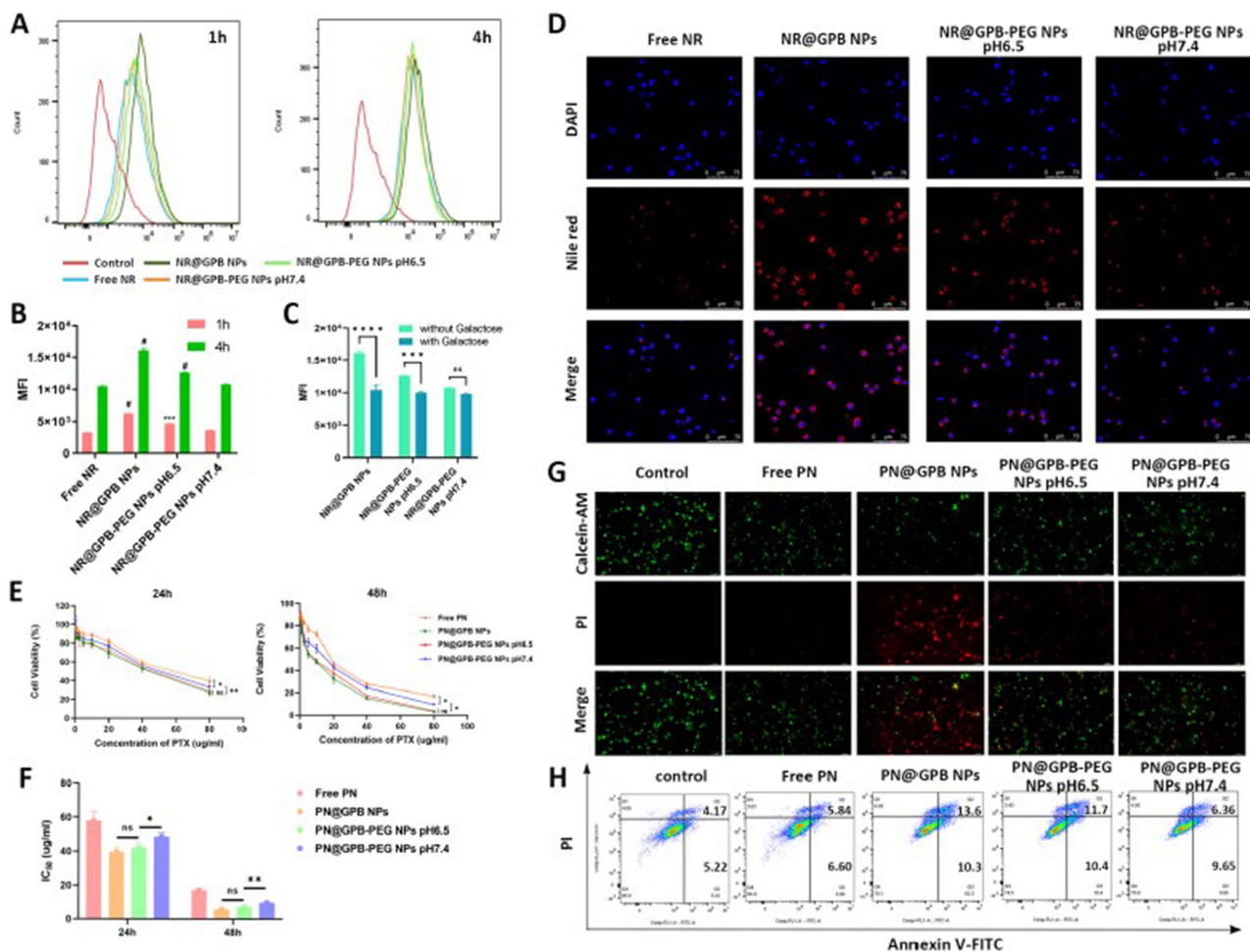


**Figure 2** In vitro cellular uptake and cytotoxicity. (A and B) Flow cytometry analysis of cellular uptake of Nile red-labeled nanoparticles in Hepa 1–6 cells. (C) Cellular uptake of Nile red-labeled nanoparticles after incubation with galactose. (D) CLSM observation of cellular uptake in Hepa 1–6 cells for 4h. (E) Cell viability of tumor cells received different treatments for 24h and 48h. (F) IC<sub>50</sub> values of different nanoformulations. (G) Fluorescence microscopic images of live (green)/dead (red) staining of Hepa 1–6 cells treated with different PTX formulations. (H) Annexin V-FITC/PI staining of tumor cells treated with different preparations. \*P<0.05, \*\*P<0.01, \*\*\*P<0.001 and \*\*\*\*P<0.0001.

internalization in tumor cells. Additionally, the fluorescence signals were distributed throughout tumor cells, likely resulting from cargo release in response to intracellular ROS stimuli.

## In vitro Cytotoxicity Assay

The CCK-8 assay was performed to assess the cytotoxic effects of various formulations on Hepa 1–6 cells, with the findings illustrated in Figure 2E. The combination of PTX and NLG919 (PN) significantly reduced the viability of tumor cells, likely due to the apoptosis-inducing properties of PTX rather than NLG919, as noted in a previous report.<sup>29</sup> Additionally, PN@GPB NPs markedly inhibited tumor cell proliferation compared to free drugs, attributed to the enhanced cellular uptake mediated by galactose. The incorporation of PBA-PEG diminished these inhibitory effects. Whereas PEG detachment and galactose exposure at pH 6.5 increased the cytotoxicity of PN@GPB-PEG NPs against tumor cells. Interestingly, no visible difference in cell viability was observed between PN@GPB-PEG NPs at pH 6.5 and PN@GPB NPs. At pH 6.5, IC<sub>50</sub> values of PN@GPB-PEG NPs were 42.15 ± 3.25 μg/mL for 24 hours and 7.21 ± 0.14 μg/mL for 48 hours, which were comparable to PN@GPB NPs but lower than the values recorded at neutral pH (Figure 2F). Overall, these findings indicated that PEG shielding and galactose exposure at pH 6.5 enhanced cellular uptake and inhibited the proliferation of tumor cells.



To visually assess inhibitory effects of PN@GPB-PEG NPs, calcein-AM and propidium iodide (PI) staining was performed. Viable cells emitted green signals while red fluorescence indicated dead or late apoptotic cells (Figure 2G). PN@GPB-PEG NPs at pH 6.5 and PN@GPB NPs treatment led to a significant presence of red signals, confirming their capacity to induce cell death in tumor cells. Furthermore, Annexin-FITC and PI staining were performed to assess apoptotic cell death. PTX induced apoptotic cell death, as indicated by an increase in total apoptotic percentage (Figure 2H). The percentage of apoptotic cells improved 1.92-fold higher for PN@GPB NPs compared to free PTX & NLG919, and even exceeded that of the resultant nanomedicines. Conversely, PN@GPB-PEG NPs at pH6.5 raised the percentage of apoptotic cells by 1.37-fold compared to pH 7.4, aligning with the CCK-8 findings.

## Immunogenic Cell Death

Encouraged by the ability of PTX to enhance tumor immunogenicity, we further investigated the events of immunogenic cell death (ICD), focusing on CRT exposure, HMGB1 and ATP release. As illustrated in Figure 3A–C, tumor cells treated with PN@GPB-PEG NPs exhibited significant CRT upregulation. PN@GPB-PEG at pH 6.5 led to an increase in CRT levels in Hepa 1–6 cells, implying that galactose exposure and PEG detachment can enhance the immunogenicity of tumor cells. HMGB1 interacts with TLR4 receptor to facilitate the antigen presentation and maturation of dendritic cells, while ATP also enhances their recruitment by activating P2RY2.<sup>12,30</sup> Therefore, we simultaneously measured HMGB1 and ATP levels. Hepa 1–6 cells exposed to PN@GPB-PEG NPs in an acidic environment exhibited elevated production of HMGB1 and ATP (Figure 3D and E). These findings suggest that PN@GPB-PEG NPs improved immunogenicity of cancer cells in a mildly acidic environment.

Next, we assessed whether above tumor cells could activate dendritic cells (DCs) *in vitro*. As shown in Figure 3H–K, all formulations containing PTX significantly enhanced the expression of CD80, CD86, and MHC II, indicating a marked activation of DCs compared to the control group. This effect may be attributed to the synergistic action of PTX-induced ICD and TLR4 activation on DCs.<sup>31,32</sup> Among these formulations, PN@GPB NPs resulted in approximately 21% maturation of BMDCs, which is 1.6 times greater than that observed with PN@GPB-PEG NPs. Furthermore, tumor cells pretreated with PN@GPB-PEG NPs at pH 6.5 achieved a higher number of mature BMDCs, leading to a 1.2- to 1.36-fold improvement in comparison with pH7.4.

Activated BMDCs have the capability to engulf and present antigens to T lymphocytes.<sup>33</sup> To investigate the activation of naïve T cells, carboxyfluorescein diacetate succinimidyl ester (CFSE)-labeled splenocytes were co-cultured with above BMDCs. As illustrated in Figure 3L and M, PN@GPB NPs exhibited the most significant reduction in CFSE of fluorescence intensity, with ~26% decrease compared to PN@GPB-PEG NPs at pH7.4. Interestingly, a mildly acidic incubation resulted in a 1.1-fold increase in T cell proliferation relative to pH 7.4, suggesting efficient T cell response initiation. It is important to highlight that all paclitaxel (PTX) formulations led to substantial T cell proliferation compared to the control group, emphasizing their potential to promote T cell-mediated tumor immunity.

## In vitro IDO Activity

Activated cytotoxic T lymphocytes concurrently produce IFN- $\gamma$ , which is crucial for T cell-based tumor immunotherapy.<sup>34</sup> However, IFN- $\gamma$  can also induce the expression of IDO1 in tumor cells, thereby negating antitumor immune responses.<sup>33</sup> It seems reasonable to simultaneously combine chemotherapy with IDO inhibition. Although NLG919 incubation had no significant effect on IDO expression (Figure 3F), these formulations significantly decreased the Kyn level (Figure 3G). Moreover, PN@GPB-PEG NPs at pH 6.5 resulted in a greater reduction of Kyn compared to a neutral pH environment. These findings confirm that PN@GPB-PEG NPs can effectively inhibit IDO activity.

## In vivo Imaging Assay

To explore *in vivo* biodistribution, Hepa 1–6 tumor-bearing mouse model was established and intravenously injected with DiR-labeled nanoparticles. Figure 4A showed that the fluorescent signals primarily displayed in the liver and spleen rather than the tumor during the 48-hour observation period. In contrast, a distinct fluorescent signal was detected at the tumor site 12 hours in DiR@GPB NPs and DiR@GPB-PEG NPs groups, with the signal intensity increasing over the 48-hour period. These findings suggest that our nanocarrier significantly enhances the accumulation of loaded drugs in tumors. DiR@GPB-PEG NPs displayed higher accumulation in tumor area compared to non-PEG NPs (Figure 4A–C).

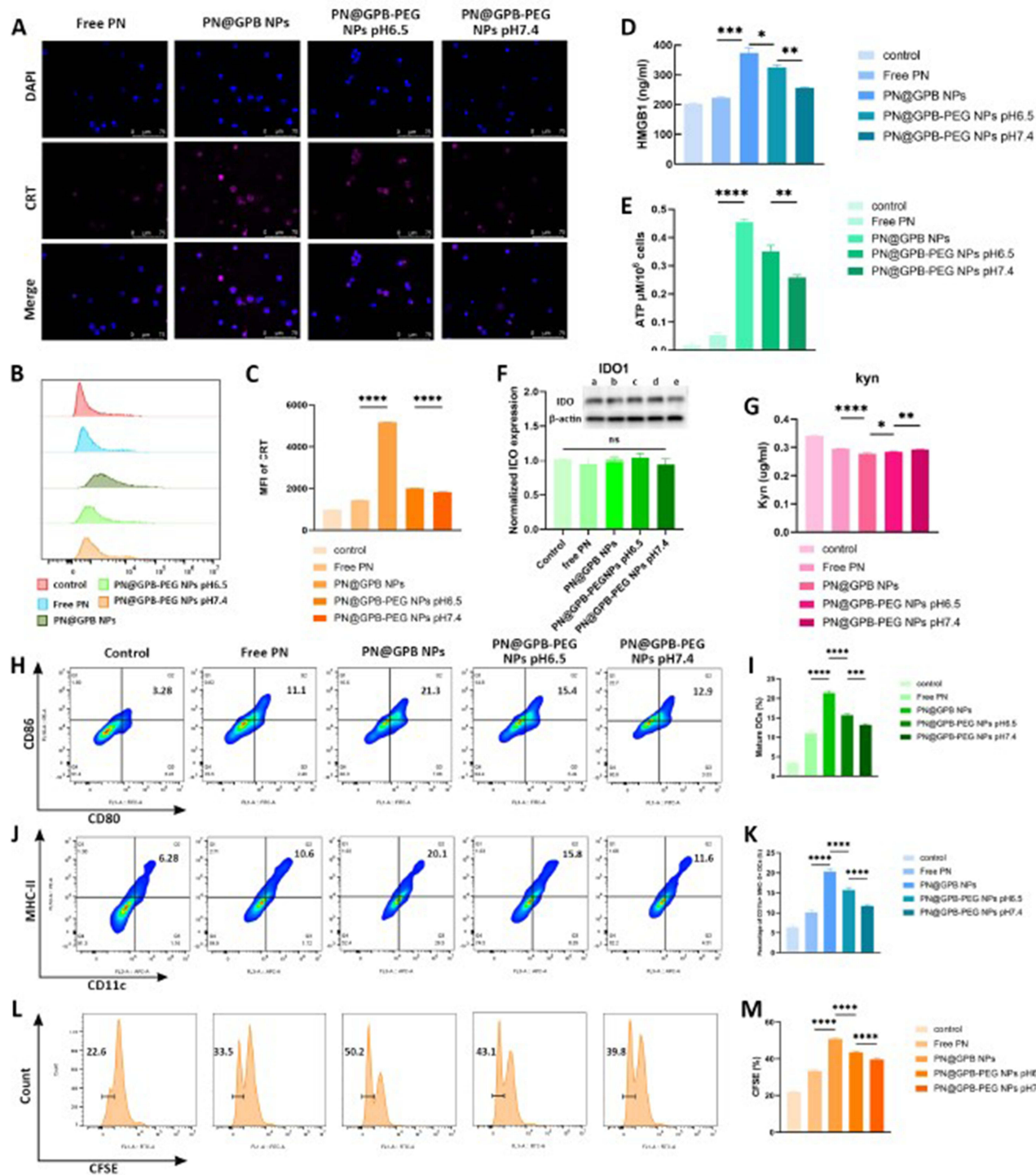


**Figure 3** In vitro immune activation. (A) Immunofluorescent staining of CRT (red) on Hepa 1–6 cells after various treatments. (B and C) Flow cytometry and analysis of CRT exposure on Hepa 1–6 cells after incubation with different formulations. (D and E) Quantitative analysis of HMGB1 and ATP release in the culture supernatant of Hepa 1–6 cells after different treatments. (F) Immunoblotting assay and semi-quantification of IDO expression in tumor cells treated with different formulations (a: control, b: PTX +NLG919, c: PN@GPB NPs, d: PN@GPB-PEG NPs pH6.5 and e:PN@GPB-PEG NPs pH7.4). (G) Kyn level in Hepa 1–6 cells receiving different treatments. (H–K) CD86, CD80 and MHC II expression and analysis on BMDCs after incubation with Hepa 1–6 cells. (L and M) The fluorescence recession and analysis of CFSE-labeled CD8+ T cells after co-incubation with above DCs. \*P<0.05, \*\*P<0.01, \*\*\*P<0.001 and \*\*\*\*P<0.0001.

This indicates that the PEG-coating and detachment reduced liver clearance while increased tumor-specific distribution. Moreover, DiR-labeled formulations showed no obvious distribution in TDLN. Together, our carrier demonstrated excellent tumor-targeting capability.

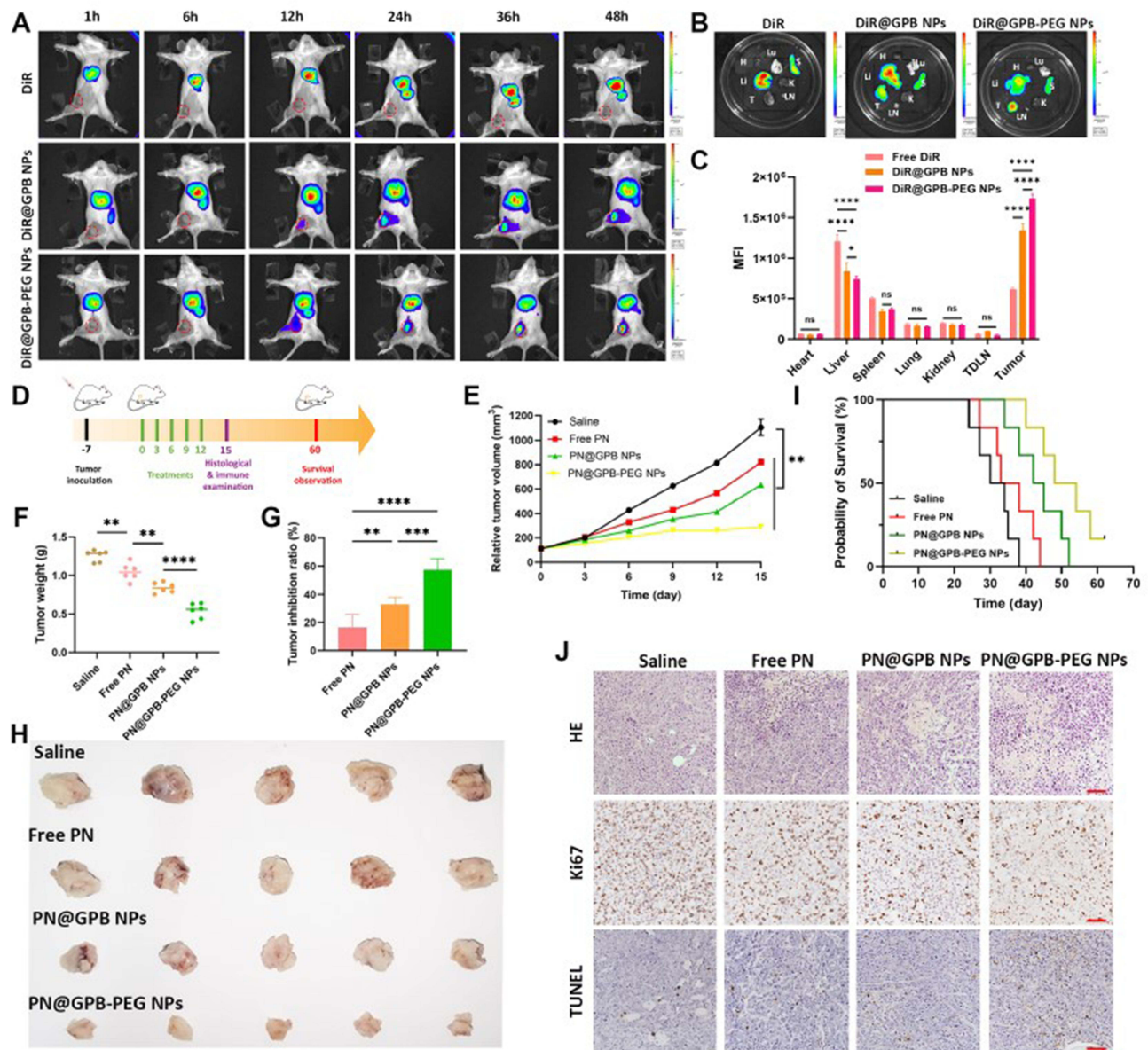


**Figure 4** In vivo biodistribution and antitumor evaluation. **(A)** In vivo fluorescence images of mice received DiR labeled nanoparticles. **(B and C)** Ex vivo fluorescence images and analysis of tumor and main organs (H: heart, Li: liver, (T) tumor, Lu: lung, (S) spleen, (K) Kidney, LN: tumor draining lymph node). **(D)** Therapeutic schedule of Hepa 1–6 tumor bearing mice. **(E)** Tumor growth curves of mice with different treatments. **(F and G)** Excised tumor weight and inhibition ratio in different treatment groups. **(H)** Represents images of tumor from mice treated with different nanoparticles. **(I)** Survival curves of mice receiving different formulations. **(J)** HE, Ki67 and TUNEL staining of Hepa 1–6 tumor tissues collected from different treatment groups. \* $P < 0.05$ , \*\* $P < 0.01$ , \*\*\* $P < 0.001$  and \*\*\*\* $P < 0.0001$ .

## In vivo Antitumor Effects

In vivo antitumor efficacy was tested in a Hepa 1–6 tumor-bearing C57BL/6 mouse model. Seven days post-tumor implantation, the mice were intravenously administered with different preparations (Figure 4D). PN moderately suppresses tumor growth with a tumor volume of  $819.7 \text{ mm}^3$  (~26%) in contrast to the saline group's  $1105.5 \text{ mm}^3$ . PN@GPB NPs demonstrated significant antitumor effects compared to PTX+NLG919, showing approximately 22% reduction in tumor volume by the 15th day. Notably, PN@GPB-PEG NPs exhibited the strongest antitumor effects with 54.3% decrease in tumor volume in comparison with PN@GPB NPs (Figure 4E). The representative images and tumor weights are presented in Figure 4F–H, confirming the effective antitumor effects of PN@GPB-PEG NPs. Figure 4I showed that PN@GPB-PEG NPs significantly extended survival compared to other reference formulations.

To further evaluate pathohistological changes, tumors were processed for HE, Ki67 and TUNEL staining. The results were shown in Figure 4J. Saline group displayed hypercellular region and nuclear polymorphism according to HE staining. For comparison, PTX+NLG919 demonstrated a slight inhibitory effect in tumor growth, which may be attributed to their weak tumor accumulation. On the contrast, PN@GPB NPs and PN@GPB-PEG NPs displayed serious necrotic and apoptotic area characterized by a large void space and cytoplasmic karyorrhexis. Evidently, PN@GPB-PEG NPs achieved the most apoptotic cells and lowest proliferation percentage, confirming the good antitumor ability of the PEG-coated galactose nanocarriers.

## In vivo Immune Responses

To explore in vivo immune responses, IHC staining and flow cytometry were carried out. PN@GPB-PEG NPs led to a significant increase in CRT expression, suggesting a high number of tumor cells undergoing ICD (Figure 5A and B).

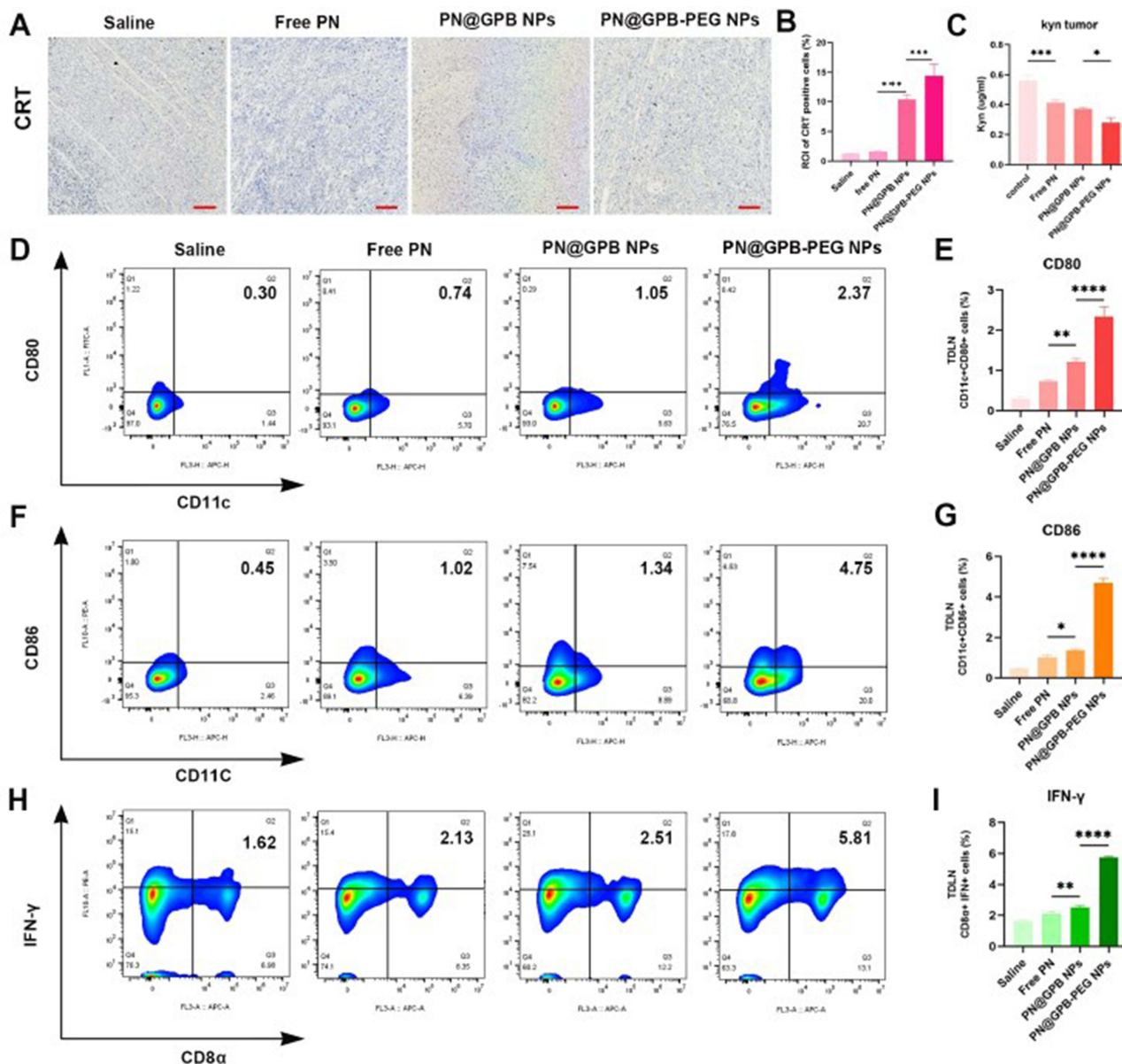


**Figure 5** In vivo immune responses. (A and B) CRT expression and analysis in tumor tissues obtained from different treatment groups. (C) Kyn level in tumors of Hepa 1–6 tumor-bearing mice following different treatments. (D–G) Flow cytometry analysis of CD80 and CD86 expression on DCs (CD11c<sup>+</sup> cells) in TDNLs. (H and I) Flow cytometry analysis of activated CD8<sup>+</sup>T cells (CD8<sup>+</sup>IFN- $\gamma$ <sup>+</sup> cells) in TDNL. \*P<0.05, \*\*P<0.01, \*\*\*P<0.001 and \*\*\*\*P<0.0001.

These DAMPs can be transported to TDLN to activate residual DCs.<sup>35,36</sup> Alternatively, the DAMPs can in situ activate DCs that subsequently migrate to TDLN.<sup>37</sup> Figure 5D–G showed that PN treatment resulted in 2.3–2.5-fold increase in CD80 and CD86 expression compared to control group, suggesting PTX-mediated DC activation. PN@GPB-PEG NPs demonstrated 2.23-fold higher DC maturity than PN@GPB NPs. Consequently, the percentage of IFN- $\gamma$ +CD8+ T cells significantly increased after PN@GPB-PEG NPs treatment, showing 2.3-fold increase compared to PN@GPB NPs (Figure 5H and I). These findings confirmed that the resultant nanomedicines had the capability to initiate adaptive immune responses.

To assess intratumoral immune responses, CD8+ T cells and other immune cells were also examined. PN@GPB-PEG NPs enhanced CD8+ T cell infiltration, with 2.2–3.1-fold increases than PN@GPB NPs and PTX+NLG919 (Figure 6A). This suggested that PN@GPB-PEG NPs boosted immune responses against tumor. However, IDO can convert tryptophan to kynurenine, promoting immune escape of tumor cells. Since NLG919 cannot inhibit IDO expression, the Kyn level was tested

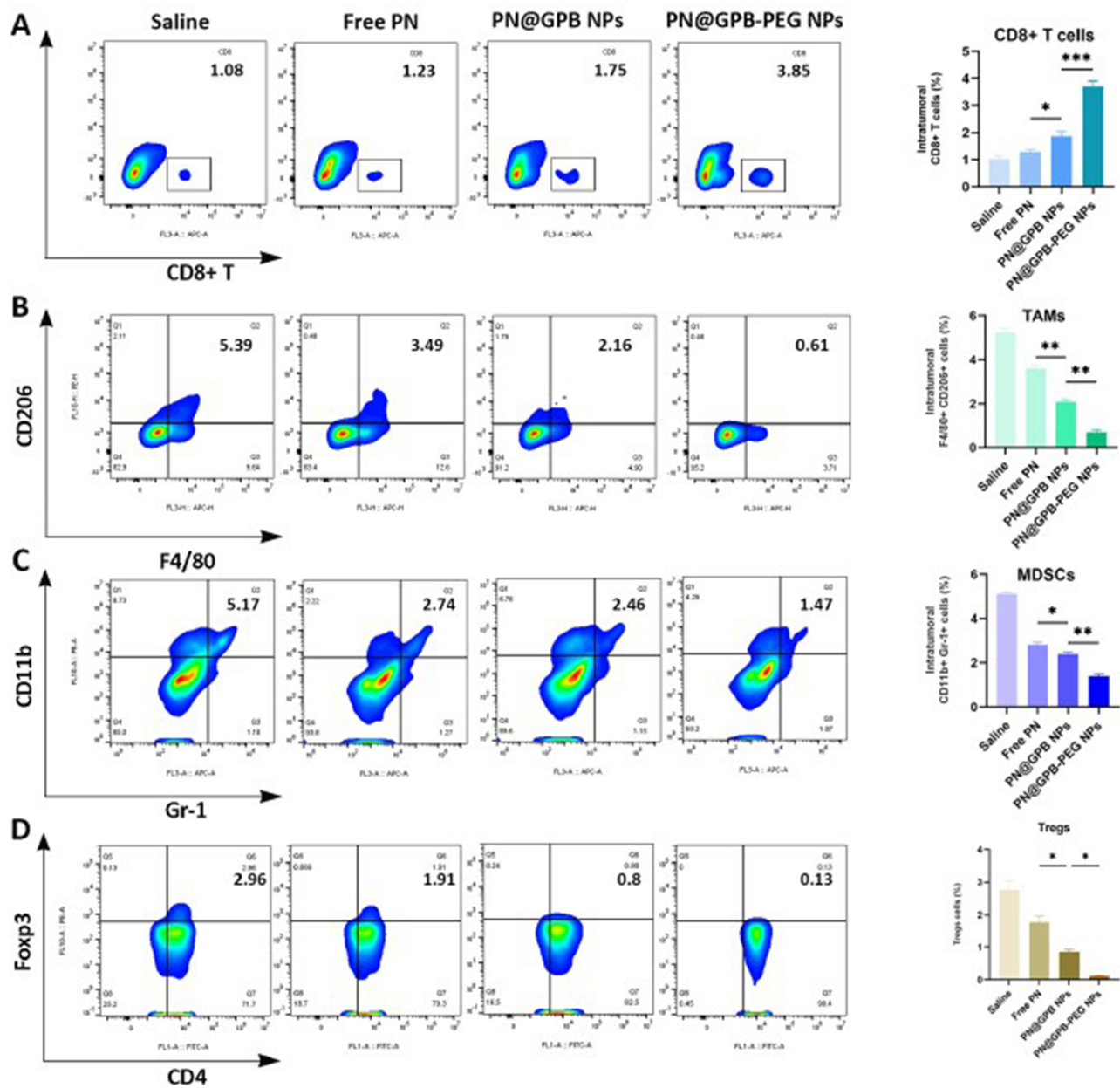


**Figure 6** Intratumoral immune components analysis. (A–H) Representative flow cytometry profiles and quantitation assay of CD8+ T cells (CD8+), TAMs (F4/80<sup>+</sup>CD206<sup>+</sup>), MDSCs (CD11b<sup>+</sup>Gr-1<sup>+</sup>) and Tregs (CD4<sup>+</sup>CD25<sup>+</sup>FoxP3<sup>+</sup>) in tumor tissues after the indicated treatments. \* $p < 0.05$ , \*\* $p < 0.001$  and \*\*\* $p < 0.0001$ .

using HPLC method.<sup>11</sup> PN@GPB-PEG NPs significantly decreased Kyn concentration (Figure 5C). As a result, Figure 6D indicated that PN@GPB-PEG NPs decreased Tregs infiltration, showing ~90% reduction in comparison with the control group. IDO can inhibit immune responses through promoting TAMs and MDSCs infiltration.<sup>38</sup> PN@GPB-PEG NPs obviously decreased TAMs' and MDSCs' infiltration (Figure 6B and C). These results collectively indicated that PN@GPB-PEG NPs could intervene ITME with the reduction of Tregs, TAMs, and MDSCs.

## Postoperative HCC Recurrence

From above results, PN@GPB-PEG NPs effectively enhanced immune responses and intervened ITME against primary tumor. Nonetheless, the high recurrence rate remains a significant barrier for the long-term survival of patients after HCC resection.<sup>39</sup> Therefore, we further investigated whether PN@GPB-PEG NPs could inhibit postsurgical HCC recurrence. Figure 7A showed that PTX formulations all reduced HCC relapse. Among these, PN@GPB-PEG NPs displayed the smallest tumor volume. The spleens were also harvested for central ( $T_{CM}$ ,  $CD44^+CD62L^+$ ) and effector memory  $CD8^+$  T cells ( $T_{EM}$ ,  $CD44^+CD62L^-$ ) analysis. PN@GPB-PEG NPs increased  $T_{EM}$  and  $T_{CM}$  proportion, 1.5~2.5-fold improvements compared to reference formulations (Figure 7B–D). Therefore, the data indicated that our nanocarrier could boost long-term immune memory and effectively reduced postoperative HCC recurrence.

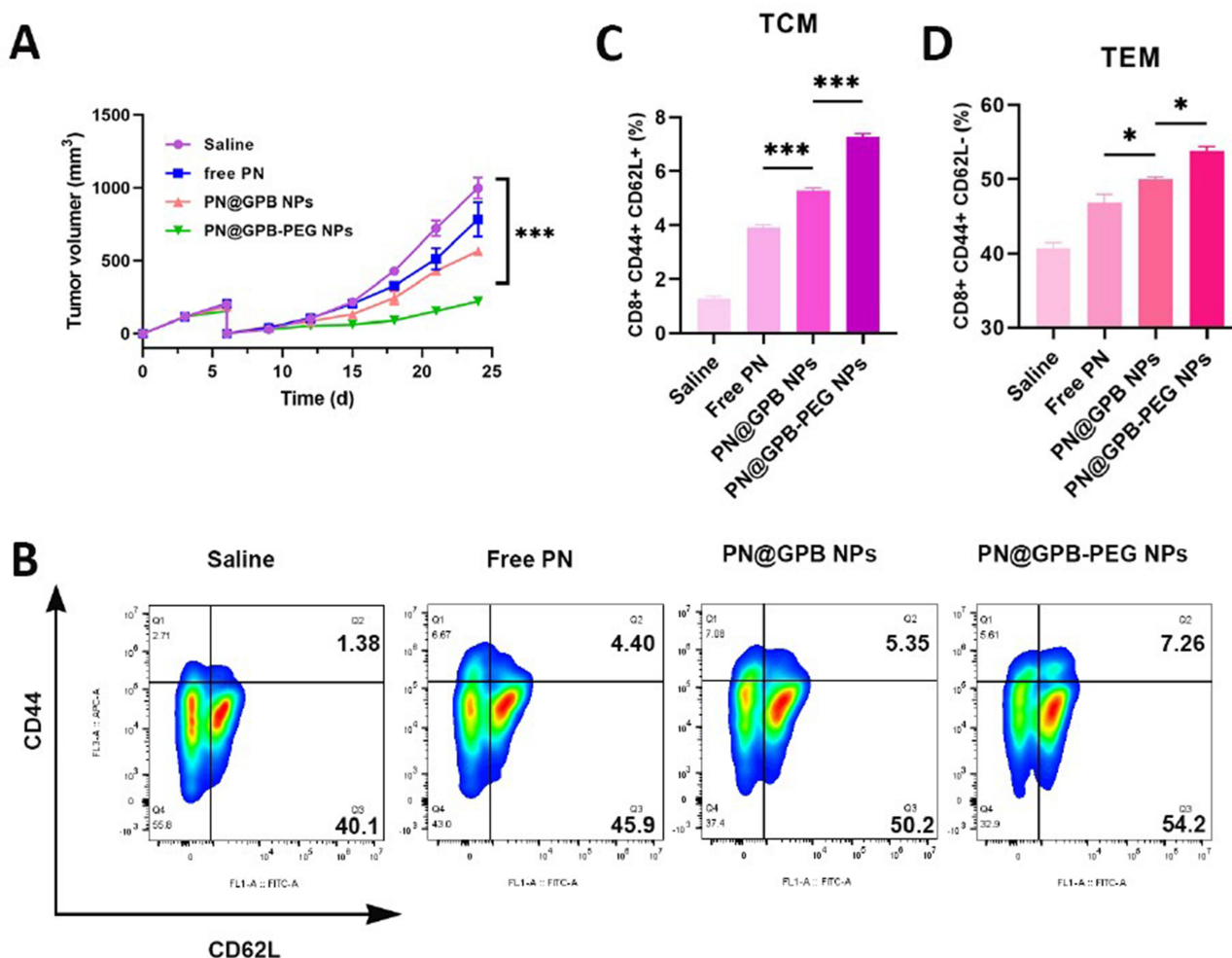


**Figure 7** In vivo therapeutic efficacy against postoperative HCC recurrence. (A) Tumor growth curves after resection in different treatment groups. (B–D) Flow cytometry plots and quantitative analysis of central (TCM) and effector memory  $CD8^+$  T cells (TEM) in the spleen of mice received different formulations. \* $p < 0.05$  and \*\*\* $p < 0.0001$ .

## Biosafety Evaluation

The biosafety was assessed by body weight and histological evaluation. From [Figures S7](#) and [S8](#), we found no significant differences in body weight or histological damage in major organs, further confirming the biocompatibility of our nanocarrier.

## Conclusion

To conclude, we developed a dual stimulus-responsive drug delivery system encapsulating PTX and NLG919 for HCC chemoimmunotherapy. The results showed that our carrier demonstrated improved accumulated in tumors, facilitated high cellular uptake in cancer cells, and released PTX and NLG919 intracellularly. The nanoformulations promoted tumor immunogenicity and suppressed IDO activity, leading to effective immune responses and ITME modulation. This combination greatly inhibited primary tumor growth and postoperative recurrence of HCC. Our findings suggest that PTX and NLG919 co-delivery could be a promising strategy for HCC chemoimmunotherapy.

## Acknowledgments

The authors acknowledge the financial support from National Natural Science Foundation of China (grant No. 82101457), Shandong Provincial Natural Science Foundation (ZR2021QH218), the Innovation Team of the Youth Innovation and Technology Program of Shandong Province (2022KJ146), Bethune Charitable Foundation (J202301E034) and Qingdao Post-doctoral Funding Program.

This paper has been uploaded to “research square” as a preprint. Link: <https://doi.org/10.21203/rs.3.rs-3329436/v1>. Our study complies with the Declaration of Helsinki.

## Author Contributions

All authors made a significant contribution to the work reported, whether that is in the conception, study design, execution, acquisition of data, analysis and interpretation, or in all these areas; took part in drafting, revising or critically reviewing the article; gave final approval of the version to be published; have agreed on the journal to which the article has been submitted; and agree to be accountable for all aspects of the work.

## Disclosure

There are no interest conflicts.

## References

1. Vogel A, Meyer T, Sapisochin G, Salem R, Saborowski A. Hepatocellular carcinoma. *Lancet*. 2022;400(10360):1345–1362. doi:10.1016/S0140-6736(22)01200-4
2. Hu Y, Chen L, Liu M, et al. Multifunctional immunotherapeutic gel prevented postoperative recurrence of hepatocellular carcinoma. *Chem Eng J*. 2023;457:141124. doi:10.1016/j.cej.2022.141124
3. Song C, Zhang J, Wen R, et al. Improved anti-hepatocellular carcinoma effect by enhanced co-delivery of Tim-3 siRNA and sorafenib via multiple pH triggered drug-eluting nanoparticles. *Mater Today Bio*. 2022;16:100350. doi:10.1016/j.mtbio.2022.100350
4. Li B, Zhang X, Wu Z, et al. Reducing postoperative recurrence of early-stage hepatocellular carcinoma by a wound-targeted nanodrug. *Adv Sci*. 2022;9(20):2200477. doi:10.1002/advs.202200477
5. Foerster F, Gairing SJ, Ilyas SI, Galle PR. Emerging immunotherapy for HCC: a guide for hepatologists. *Hepatology*. 2022;75(6):1604–1626. doi:10.1002/hep.32447
6. Zhou Z, Li X, Yang G, et al. Targeting  $\beta$ -catenin and PD-L1 simultaneously by a racemic supramolecular peptide for the potent immunotherapy of hepatocellular carcinoma. *Theranostics*. 2023;13(10):3371–3386. doi:10.7150/thno.83377
7. Wang Y, Qian J, Xu W, et al. Polysaccharide nanodons for photochemotherapy-amplified immunogenic cell death to potentiate systemic antitumor immunity against hepatocellular carcinoma. *Adv Funct Mater*. 2023;33(5):2208486. doi:10.1002/adfm.202208486
8. Fumet J-D, Limagne E, Thibaudin M, Ghiringhelli F. Immunogenic cell death and elimination of immunosuppressive cells: a double-edged sword of chemotherapy. *Cancers*. 2020;12(9):2637. doi:10.3390/cancers12092637
9. Wang Q, Ju X, Wang J, Fan Y, Ren M, Zhang H. Immunogenic cell death in anticancer chemotherapy and its impact on clinical studies. *Cancer Lett*. 2018;438:17–23. doi:10.1016/j.canlet.2018.08.028
10. Wang XF, Wang HS, Wang H, et al. The role of indoleamine 2,3-dioxygenase (IDO) in immune tolerance: focus on macrophage polarization of THP-1 cells. *Cell Immunol*. 2014;289(1–2):42–48. doi:10.1016/j.cellimm.2014.02.005

11. Song JX, Cheng MY, Xie Y, Li KK, Zang XL. Efficient tumor synergistic chemoimmunotherapy by self-augmented ROS-responsive immunomodulatory polymeric nanodrug. *J Nanobiotechnol.* 2023;21(1). doi:10.1186/s12951-023-01842-1
12. Luo K, Lian Y, Zhang M, Yu H, Wang G, Li J. Charge convertible biomimetic micellar nanoparticles for enhanced melanoma-targeted therapy through tumor cells and tumor-associated macrophages dual chemotherapy with IDO immunotherapy. *Chem Eng J.* 2021;412:128659. doi:10.1016/j.cej.2021.128659
13. Zang X, Song J, Yi X, Piyu J. Polymeric indoximod based prodrug nanoparticles with doxorubicin entrapment for inducing immunogenic cell death and improving the immunotherapy of breast cancer. *J Mat Chem B.* 2022;10(12):2019–2027. doi:10.1039/D2TB00197G
14. Hu C, Song Y, Zhang Y, et al. Sequential delivery of PD-1/PD-L1 blockade peptide and IDO inhibitor for immunosuppressive microenvironment remodeling via an MMP-2 responsive dual-targeting liposome. *Acta Pharmaceutica Sinica B.* 2023;13(5):2176–2187. doi:10.1016/j.apsb.2023.02.009
15. Du X, Hou Y, Huang J, et al. Cytosolic delivery of the immunological adjuvant Poly I:C and cytotoxic drug crystals via a carrier-free strategy significantly amplifies immune response. *Acta Pharmaceutica Sinica B.* 2021;11(10):3272–3285. doi:10.1016/j.apsb.2021.03.014
16. Sakellari GI, Zafeiri I, Pawlik A, et al. Independent co-delivery of model actives with different degrees of hydrophilicity from oil-in-water and water-in-oil emulsions stabilised by solid lipid particles via a Pickering mechanism: a-proof-of-principle study. *J Colloid Interface Sci.* 2021;587:644–649. doi:10.1016/j.jcis.2020.11.021
17. Li X, Chen G, Wang Y, et al. Systematic co-delivery of dual agonists to enhance cancer immunotherapy. *Nano Res.* 2022;15(9):8326–8335. doi:10.1007/s12274-022-4504-2
18. Moncal KK, Tigli Aydın RS, Godzik KP, et al. Controlled co-delivery of pPDGF-B and pBMP-2 from intraoperatively bioprinted bone constructs improves the repair of calvarial defects in rats. *Biomaterials.* 2022;281:121333. doi:10.1016/j.biomaterials.2021.121333
19. Gao Q, Feng J, Liu W, et al. Opportunities and challenges for co-delivery nanomedicines based on combination of phytochemicals with chemotherapeutic drugs in cancer treatment. *Adv Drug Delivery Rev.* 2022;188:114445. doi:10.1016/j.addr.2022.114445
20. Li F, Song NC, Dong YH, et al. A proton-activatable DNA-based nanosystem enables co-delivery of CRISPR/Cas9 and DNAzyme for combined gene therapy. *Angew Chem-Int Ed.* 2022;61(9):e202116569.
21. Dang H, Tian Y, Cheng Q, Teng C, Xie K, Yan L. Galactose conjugated boron dipyrromethene and hydrogen bonding promoted J-aggregates for efficiently targeted NIR-II fluorescence assistant photothermal therapy. *J Colloid Interface Sci.* 2022;612:287–297. doi:10.1016/j.jcis.2021.12.177
22. Chen WZ, Zhen X, Wu W, Jiang XQ. Responsive boron biomaterials and their biomedical applications. *Sci China-Chem.* 2020;63(5):648–664. doi:10.1007/s11426-019-9699-3
23. Badea I, Ciutaru D, Lazar L, Nicolescu D, Tudose A. Rapid HPLC method for the determination of paclitaxel in pharmaceutical forms without separation. *J Pharm Biomed Anal.* 2004;34(3):501–507. doi:10.1016/S0731-7085(03)00628-9
24. Yu N, Ding M, Wang F, et al. Near-infrared photoactivatable semiconducting polymer nanocomplexes with bispecific metabolism interventions for enhanced cancer immunotherapy. *Nano Today.* 2022;46:101600. doi:10.1016/j.nantod.2022.101600
25. Karimi S, Bagher Z, Najmoodin N, Simorgh S, Pezeshki-Modaress M. Alginate-magnetic short nanofibers 3D composite hydrogel enhances the encapsulated human olfactory mucosa stem cells bioactivity for potential nerve regeneration application. *Int J Biol Macromol.* 2021;167:796–806. doi:10.1016/j.ijbiomac.2020.11.199
26. Chen Q, Wang C, Zhang X, et al. In situ sprayed bioresponsive immunotherapeutic gel for post-surgical cancer treatment. *Nature Nanotechnol.* 2019;14(1):89–97. doi:10.1038/s41565-018-0319-4
27. Heyder RS, Sunbul FS, Almuqbil RM, Fines CB, da Rocha SRP. Poly(anhydride-ester) gemcitabine: synthesis and particle engineering of a high payload hydrolysable polymeric drug for cancer therapy. *J Control Release.* 2021;330:1178–1190. doi:10.1016/j.jconrel.2020.11.025
28. Cao J, Gao X, Cheng M, et al. Reversible shielding between dual ligands for enhanced tumor accumulation of ZnPc-Loaded micelles. *Nano Lett.* 2019;19(3):1665–1674. doi:10.1021/acs.nanolett.8b04645
29. Xu J, Ren X, Guo T, et al. NLG919/cyclodextrin complexation and anti-cancer therapeutic benefit as a potential immunotherapy in combination with paclitaxel. *Eur J Pharm Sci.* 2019;138:105034. doi:10.1016/j.ejps.2019.105034
30. Nystrom S, Antoine DJ, Lundback P, et al. TLR activation regulates damage-associated molecular pattern isoforms released during pyroptosis. *EMBO J.* 2013;32(1):86–99. doi:10.1038/emboj.2012.328
31. Pfannenstiel LW, Lam SSK, Emens LA, Jaffee EM, Armstrong TD. Paclitaxel enhances early dendritic cell maturation and function through TLR4 signaling in mice. *Cell Immunol.* 2010;263(1):79–87. doi:10.1016/j.cellimm.2010.03.001
32. Luo K, Yang L, Yan C, et al. A dual-targeting liposome enhances triple-negative breast cancer chemoimmunotherapy through inducing immunogenic cell death and inhibiting STAT3 activation. *Small.* 2023;19:2302834. doi:10.1002/smll.202302834
33. Song P, Han X, Li X, et al. Bacteria engineered with intracellular and extracellular nanomaterials for hierarchical modulation of antitumor immune responses. *Mater Horiz.* 2023;10(8):2927–2935. doi:10.1039/D3MH00249G
34. Takeda K, Nakayama M, Hayakawa Y, et al. IFN- $\gamma$  is required for cytotoxic T cell-dependent cancer genome immunoeediting. *Nat Commun.* 2017;8(1):14607. doi:10.1038/ncomms14607
35. Ma X, Yang S, Zhang T, et al. Bioresponsive immune-booster-based prodrug nanogel for cancer immunotherapy. *Acta Pharmaceutica Sinica B.* 2022;12(1):451–466. doi:10.1016/j.apsb.2021.05.016
36. Ren H, Yong J, Yang Q, et al. Self-assembled FeS-based cascade bioreactor with enhanced tumor penetration and synergistic treatments to trigger robust cancer immunotherapy. *Acta Pharmaceutica Sinica B.* 2021;11(10):3244–3261. doi:10.1016/j.apsb.2021.05.005
37. Sun Z, Deng G, Peng X, et al. Intelligent photothermal dendritic cells restart the cancer immunity cycle through enhanced immunogenic cell death. *Biomaterials.* 2021;279:121228. doi:10.1016/j.biomaterials.2021.121228
38. Campesato LF, Budhu S, Tchaicha J, et al. Blockade of the AHR restricts a Treg-macrophage suppressive axis induced by L-Kynurenine. *Nat Commun.* 2020;11(1). doi:10.1038/s41467-020-17750-z
39. Zhang X-P, Chen X-J, Li B-Z, et al. Active targeted Janus nanoparticles enable anti-angiogenic drug combining chemotherapy agent to prevent postoperative hepatocellular carcinoma recurrence. *Biomaterials.* 2022;281:121362. doi:10.1016/j.biomaterials.2022.121362



International Journal of Nanomedicine

Dovepress

### Publish your work in this journal

The International Journal of Nanomedicine is an international, peer-reviewed journal focusing on the application of nanotechnology in diagnostics, therapeutics, and drug delivery systems throughout the biomedical field. This journal is indexed on PubMed Central, MedLine, CAS, SciSearch<sup>®</sup>, Current Contents<sup>®</sup>/Clinical Medicine, Journal Citation Reports/Science Edition, EMBase, Scopus and the Elsevier Bibliographic databases. The manuscript management system is completely online and includes a very quick and fair peer-review system, which is all easy to use. Visit <http://www.dovepress.com/testimonials.php> to read real quotes from published authors.

Submit your manuscript here: <https://www.dovepress.com/international-journal-of-nanomedicine-journal>